Detecting liquid contamination on surfaces using hyperspectral imaging data

Russell E. Warren[1a], David B. Cohn[b], Marc-Andre Gagnon[c], Vincent Farley[c]
[a]EO-Stat Inc., 10010 Vail Drive, Chapel Hill, NC USA 27517; [b]DBC Technology Corp., 4221 Mesa St., Torrance CA USA 90505; [c]Telops, avenue St.-Jean-Baptiste, Québec (Québec) Canada G2E 6J5

ABSTRACT

Over the past two years we have developed a new approach for detecting and identifying the presence of liquid chemical contamination on surfaces using hyperspectral imaging data. This work requires an algorithm for unmixing the data to separate the liquid contamination component of the data from all other possible spectral effects, such as the illumination and reflectance spectra of the pure background. The contamination components from S and P polarized reflectance data are then used to estimate the complex refractive index. We retain the index estimates within spectral windows chosen for each of a set of candidate contaminant materials based on their optical extinction. Spectral estimates within those windows are characteristic of the liquid material, and can be passed on to an algorithm for chemical detection and identification. The resulting algorithm is insensitive to the composition of the surface material, and requires no prior measurements of the uncontaminated surface. In a series of field tests, data from the Telops Hyper-Cam sensor were used to develop and validate our approach. We discuss our hyperspectral unmixing and index estimation approaches, and show results from tests conducted at the Telops facility in Québec under a contract with the U.S. Army Edgewood Chemical Biological Center.

Keywords: Surface contamination detection, hyperspectral imaging, refractive index, polarization

1. INTRODUCTION

Because of its importance, considerable research effort has been directed to the detection of chemical contamination on surfaces. The review paper by Petryk [1] summarizes many of the approaches tried for this problem. The approaches broadly fall into two groups: those that extract samples from the surface for analysis (contact), and standoff methods that do not make contact with the surface or its contamination. Only the latter are useful for practical field deployment. Of these, Raman scattering has probably been the most studied. Its advantages are the insensitivity to the surface composition, fast time-response for real-time implementation, and well-characterized Raman spectra for specific threat materials. However, the disadvantages of weak signal returns, particularly for small droplet contamination over extended surfaces, and the potentially large UV laser transmitter requirement have made it impractical for advanced development in addition to its being non-eyesafe. Other methods such as photoacoustic spectroscopy (PAS), photothermal-surface acoustic wave (PT-SAW), photothermal interferometry (PTI), photothermal imaging (PT), and thermal luminescence (TI) have been tried with varying success, but all suffer from sensitivity problems, and appear to require independent measurements from uncontaminated surfaces. The latter requirement is a severe limitation for practical implementation in temporally changing and *a priori* unknown collection environments.

Over the past two years under a contract with the U.S. Army Edgewood Chemical Biological Center we have been engaged in developing a new approach using hyperspectral imaging in the LWIR spectral region with the state-of-the-art Telops Hyper-Cam sensor. Our approach avoids the restrictions of existing approaches such as requiring uncontaminated surface reflection measurements or assumptions about the contaminating liquid such as its film thickness. A key step in the approach is the use of a new hyperspectral unmixing algorithm (Warren and Osher [2]) for

[1] eostatinc@aol.com; phone 919.933.3266

Chemical, Biological, Radiological, Nuclear, and Explosives (CBRNE) Sensing XVI, edited by Augustus Way Fountain III, Proc. of SPIE Vol. 9455, 94550M · © 2015 SPIE · CCC code: 0277-786X/15/$18 · doi: 10.1117/12.2176617

isolating the liquid-surface spectral component in the presence of interfering radiance sources such as the illumination source and reflection from the uncontaminated surface. The surface contamination algorithm uses polarized[2] S and P reflectance measurements of the contaminating liquid as seen on the background surface to estimate the complex refractive index of the contaminant within spectral windows chosen to maximally isolate the spectral features of the liquid while ignoring the features associated with the usually unknown background surface. The resulting algorithm is thereby insensitive to the background material. Estimates of the liquid index within these windows form the feature vectors needed for classifier training and testing. Section 2 describes the modeling and theoretical basis for the algorithm. Application to the Telops Hyper-Cam sensor data is discussed in Section 3. We summarize in Section 4.

2. THEORY

2.1 Reflectance model for liquids on surfaces

We begin the discussion of the theoretical basis for our liquid detection on surfaces approach with a summary of the polarized reflectance model of Harig, et al. [3]. Letting R denote the spectral reflectance of a possibly contaminated surface, for plane-wave thermal illumination R will be the average of the reflectances of radiation parallel R^P and perpendicular R^S to the plane of incidence:

$$R = \frac{1}{2}\left(R^P + R^S\right).$$

The Harig, et al. [3] model for R^P and R^S uses three stacked media: air, the contaminating liquid, and a background surface having refractive indices $n_1 = 1$, n_2, and n_3, where the latter two are in general complex. The radiation Poynting vector makes angles θ_1, θ_2, and θ_3 with respect to the surface normal, and the latter two angles are also generally complex.

Given θ_1, we find θ_2 and θ_3 through Snell's law:

$$\sin\theta_2 = \frac{1}{n_2}\sin\theta_1\,, \quad \sin\theta_3 = \frac{n_2}{n_3}\sin\theta_2\,.$$

Letting r_{12} and r_{23} represent the reflected complex amplitudes at the air-film and film-background interfaces for a given polarization, we find the Fresnel expressions for parallel and perpendicular polarizations from Born and Wolf [4]:

$$r_{12}^P = \frac{n_2\cos\theta_1 - \cos\theta_2}{n_2\cos\theta_1 + \cos\theta_2}\,, \quad r_{12}^S = \frac{\cos\theta_1 - n_2\cos\theta_2}{\cos\theta_1 + n_2\cos\theta_2}\,,$$
$$r_{23}^P = \frac{n_3\cos\theta_2 - n_2\cos\theta_3}{n_3\cos\theta_2 + n_2\cos\theta_3}\,, \quad r_{23}^S = \frac{n_2\cos\theta_2 - n_3\cos\theta_3}{n_2\cos\theta_2 + n_3\cos\theta_3}\,.$$

We then compute R^P and R^S using Harig, et al. [3] as

$$R^j = \left|\frac{r_{12}^j + r_{23}^j e^{2i\delta}}{1 + r_{12}^j r_{23}^j e^{2i\delta}}\right|^2\,,$$

[2] We note that Thériault, et. al. [5] have used differential polarization for mitigating sky radiance drifts, but not for estimating the refractive index.

where j denotes either P or S, and δ is the complex phase shift given by

$$\delta = \frac{2\pi d}{\lambda}\sqrt{n_2^2 - \sin^2\theta_1}\ ,$$

with d the film thickness and λ the wavelength.

The spectral reflectance model described above was implemented in Matlab and applied to the reflectance of the composite surface consisting of a film layer of the simulant SF96 added to an aluminum substrate. Figures 1 and 2 plot the refractive indices (real and imaginary) of SF96 and aluminum. We note that aluminum has a nontrivial index structure overall but is nearly linear in the LWIR spectral region. Figures 3 and 4 plot the reflectance components of SF96 and aluminum at $\theta_1 = 45^o$ incidence angle using the refractive indices shown in Figures 1 and 2. Figure 5 plots R from SF96 at 45^o incidence for various film thicknesses d: 0.01, 0.1, 1, 10, 100, and 1000 μm. The reflectances transition from those of pure Al for small thicknesses to pure SF96 at the larger thicknesses. Of particular concern are the results from d = 1 and 10 μm that bound threat levels of contamination. In this range the modeled reflectances generally look neither like SF96 or Al.

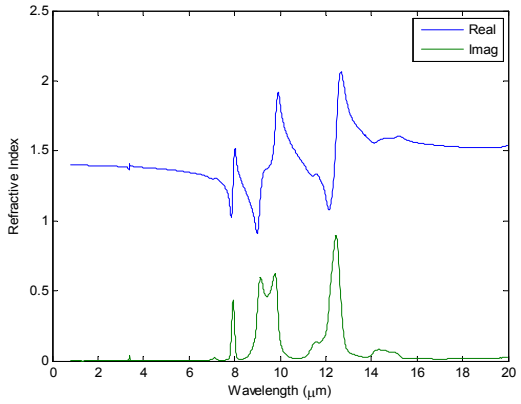

Figure 1. Complex refractive indices of SF96.

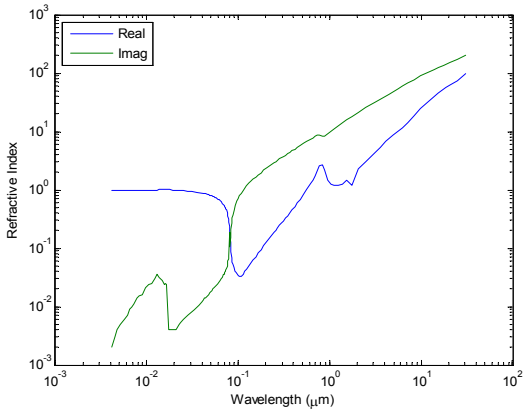

Figure 2. Complex refractive indices of Al.

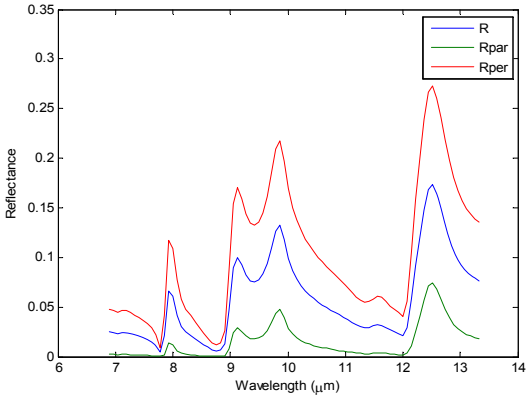

Figure 3. Reflectances of SF96 at 45^o incidence.

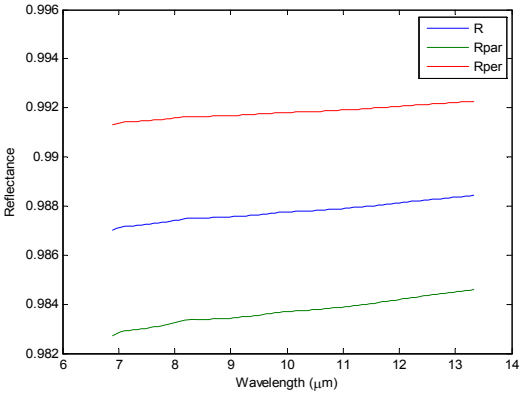

Figure 4. Reflectances of Al at 45^o incidence.

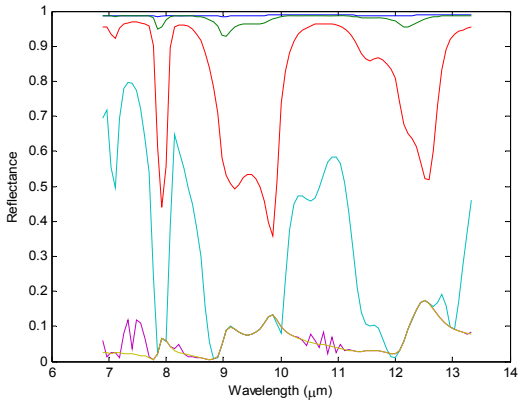

Figure 5. Unpolarized reflectances of SF96 on Al for different film thicknesses.

2.2 Surface contamination detection algorithm

As noted above, the addition of surface films such as SF96 to substrates such as aluminum is expected to produce reflectances that can be substantially different from either material alone depending on the film thickness and fractional coverage. Since these quantities and the background material are unknown in most cases, a direct approach of using the reflectance model above to fit the observed spectral reflectance is unlikely to be successful.

However, close inspection of the composite SF96-aluminum reflectances shown in Figure 5 reveals that within specific spectral regions around a narrow band near 8 μm, a broader band between 9-10 μm, and a strong band near 12.5 μm, the composite reflectance looks like that of SF96 over an extended range of film thicknesses *d* including those of tactical interest of about 5 μm. These spectral regions coincide with the stronger absorption regions of SF96 as seen in the imaginary refractive index in Figure 1. Those features suggest that within the optically thick spectral regions the observed reflectance becomes insensitive to both the background material and the specific film thickness. The idea then is to base the detection and identification approach around hyperspectral imaging data observed in spectral regions chosen for each liquid material to emphasize the components of the liquid that are independent of the background.

In order for this method to be successful, liquid agents such as VX need to have substantial absorption features in the LWIR spectral region of thermal imaging devices. Figure 6 shows that the imaginary refractive index of VX (bottom plot) does have significant absorption structure in the LWIR region.

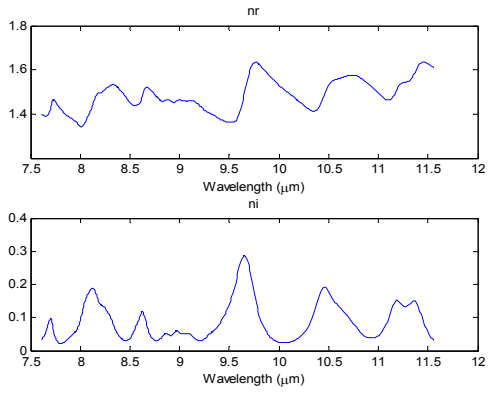

Figure 6. Real (top) and imaginary (bottom) refractive index of VX.

Building a useful detection and discrimination algorithm using hyperspectral (HS) imaging data requires other algorithmic components, viz., (1) a method for separating the spectral reflectance of the liquid-background composite from all other possible radiance components such as the illumination source and pure background reflectance, (2) a method for uniquely identifying the liquid material from the liquid-background reflectance component within high liquid absorption regions of the data, and (3) a detection and classification algorithm trained with the spectrally windowed candidate liquid materials. We address the first two components here; the third awaits further development.

With respect to the first topic, we have used a hyperspectral unmixing approach (Warren and Osher [2]), based on well-established methods on nonlinear optimization theory that requires no prior knowledge of the HS data such as training samples from the pure background. The unmixing problem is formulated as a biconvex constrained optimization with the constraints enforced by Bregman splitting. The resulting algorithm estimates the spectral and spatial structure in the image through a numerically stable iterative approach that removes the need for separate endmember and spatial abundance estimation steps.

As an example of the use of our unmixing algorithm, Figure 7 shows the three spectral reflectance components from a HS data set representing 3.3 g/m^2 of SF96 on aluminum at S-polarization. These data were collected by Telops personnel using their Hyper-Cam sensor during testing at their facility on September 19, 2013. The three components are the pure Al, quartz lamp used as the thermal illuminator, and SF96-Al composite reflectance. The measurement configuration will be described in more detail below. The corresponding spatial components (the analogue of the "abundances" in the HS literature) are shown in Figure 8, with the pure aluminum (left), lamp (center), and SF96-Al (right). Without the unmixing step the data would be a mixture of all three components making it difficult to isolate the liquid-background signature.

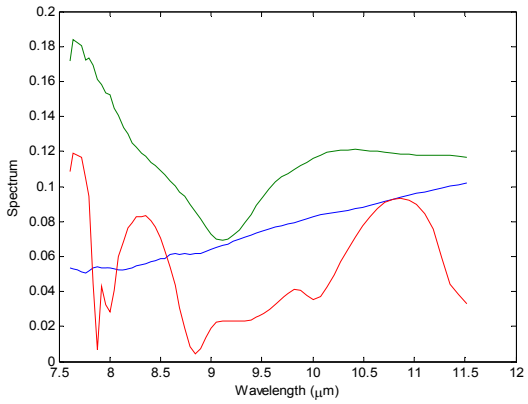

Figure 7. Spectral components from unmixing HS data: pure Al (blue), lamp (green), and SF96-Al (red) .

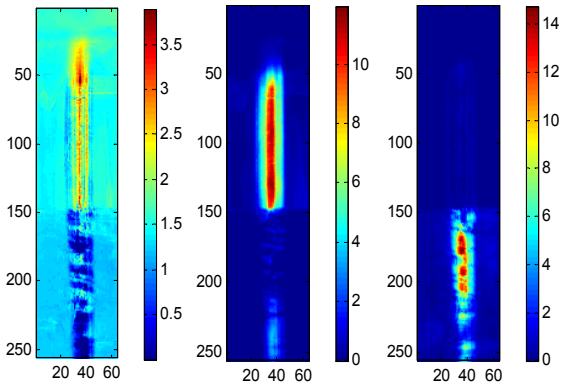

Figure 8. Spatial components from the unmixing: Al (left), lamp (center), SF96-Al (right).

Having the liquid-background component from the reflectance data, the next processing step is to extract feature vectors from the data that isolate the spectral structure of the liquid while minimizing interference from the generally unknown background surface reflectance. The use of spectral windows chosen to emphasize high absorption parts of the spectrum appears to be the best method for doing this. Having these we want the feature vectors to provide a unique "fingerprint" of the liquid for use in a classifier. The ideal information in this regard is the complex refractive index. We have developed an algorithm for estimating the complex refractive index from S and P polarized reflectance data for this purpose.

We first recapitulate the well-known model for the polarization components of thermal radiance reflected from a flat homogeneous substrate surface. Following Born and Wolf [4] we have the Fresnel expressions for reflected radiation parallel r^P and perpendicular r^S to the plane of incidence:

$$r^P = \frac{\tan(\theta_1 - \theta_2)}{\tan(\theta_1 + \theta_2)}, \qquad r^S = -\frac{\sin(\theta_1 - \theta_2)}{\sin(\theta_1 + \theta_2)},$$

where θ_1 is the incidence angle of radiation with respect to the surface normal, and θ_2 is the (complex) angle of refraction into the substrate. The latter is given by Snell's law:

$$\sin\theta_2 = \frac{1}{n_2}\sin\theta_1,$$

with n_2 the complex refractive index of the substrate material. The corresponding reflectivities are given by $R^S = \left|r^S\right|^2$ and $R^P = \left|r^P\right|^2$. Given measured spectra R_d^S and R_d^P representing R^S and R^P using polarization filtered broadband thermal radiation, our first goal is to estimate the real and imaginary parts of n_2 as a function of wavelength.

n_2 is estimated from Snell's law from estimates of $\theta_2 \equiv \phi + i\psi$. We propose the following iterative algorithm based on a complex implementation of Newton's method:

$$\phi^k = \phi^{k-1} + \gamma\left(\mathrm{Re}\left(G^P(\theta_2^{k-1})\right) + \mathrm{Re}\left(G^S(\theta_2^{k-1})\right)\right),$$
$$\psi^k = \psi^{k-1} + \gamma\left(\mathrm{Im}\left(G^P(\theta_2^{k-1})\right) + \mathrm{Im}\left(G^S(\theta_2^{k-1})\right)\right),$$

with

$$G^j\left(\theta_2^{k-1}\right) \equiv \frac{R_d^j - R^j\left(\theta_2^{k-1}\right)}{\dfrac{\partial R^j\left(\theta_2^{k-1}\right)}{\partial \theta_2}}\ ,\quad j = P, S\ .$$

Here, $\theta_2^{k-1} \equiv \phi^{k-1} + i\psi^{k-1}$, and

$$\frac{\partial R^S\left(\theta_2^{k-1}\right)}{\partial \theta_2} = -\frac{\sin\left(\theta_1 - \bar{\theta}_2^{k-1}\right)}{\sin\left(\theta_1 + \bar{\theta}_2^{k-1}\right)}\left[\frac{\cos\left(\theta_1 - \theta_2^{k-1}\right)}{\sin\left(\theta_1 + \theta_2^{k-1}\right)} + \frac{\sin\left(\theta_1 - \theta_2^{k-1}\right)\cos\left(\theta_1 + \theta_2^{k-1}\right)}{\sin^2\left(\theta_1 + \theta_2^{k-1}\right)}\right],$$
$$\frac{\partial R^P\left(\theta_2^{k-1}\right)}{\partial \theta_2} = -\frac{\tan\left(\theta_1 - \bar{\theta}_2^{k-1}\right)}{\tan\left(\theta_1 + \bar{\theta}_2^{k-1}\right)}\left[\frac{\sec^2\left(\theta_1 - \theta_2^{k-1}\right)}{\tan\left(\theta_1 + \theta_2^{k-1}\right)} + \frac{\tan\left(\theta_1 - \theta_2^{k-1}\right)}{\sin^2\left(\theta_1 + \theta_2^{k-1}\right)}\right].$$

The parameter γ is the step size for the Newton update to the estimates at the previous iteration. Experience suggests $\gamma = 0.05$ is a reasonable choice. The iterations are initialized by $\theta_2^0 = \pi/4(1+0.2i)$, for example.

The algorithm above for estimating n_2 from measurements of the reflectivities at the two polarizations was implemented in Matlab and evaluated on simulated data made by adding pseudo-random gaussian white noise of standard error 0.001 to model calculations of R^S and R^P for the simulant SF96. We used 256 wavelengths equally spaced between $\lambda_1 = 6.9\mu m$ and $\lambda_2 = 13.33\mu m$ for various incidence angles θ_1. Figure 9 compares the input and estimated refractive indices of SF96 for $\theta_1 = 70^\circ$. Figure 10 shows the input reflectivities and the model fits. The algorithm required 203 iterations to converge. The computation time was 0.07 s. Except for some noise in the estimates of the imaginary part of the index, the estimates of n_2 are quite close to the input spectra. The reflectivity fits are also close to the input data.

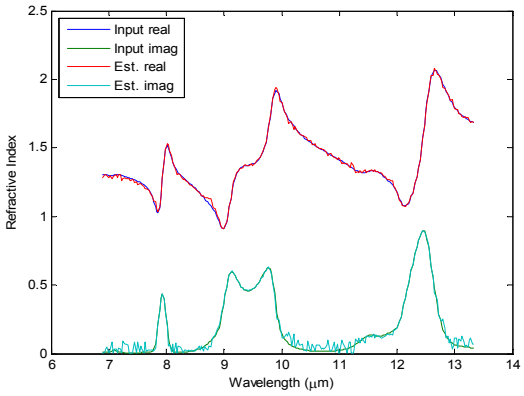

Figure 9. Real and imaginary refractive indices of SF96.

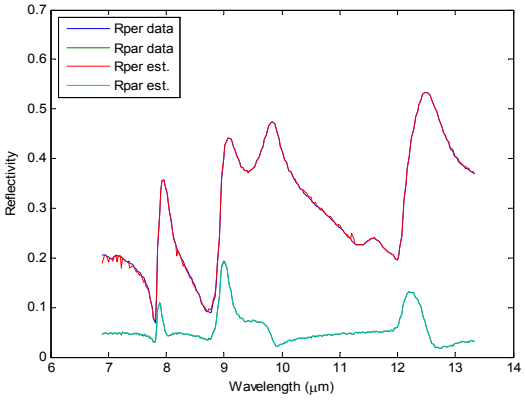

Figure 10. Reflectivity data and model fits for SF96.

3. HYPERSPECTRAL DATA COLLECTION AND PROCESSING

3.1 Data collection

In September 2013 a data collection effort at Telops Corp. was carried out to acquire hyperspectral imaging data for use in developing a prototype algorithm for detecting and discriminating liquid chemicals deposited on ambient surfaces. Data from the Telops' Hyper-Cam imaging sensor at about 70 spectral bands between 7.5-11.5 μm were collected at two polarizations, perpendicular (S) and parallel (P) to the radiation incidence plane, on two surfaces, smooth aluminum and slate. The Al data provide high SNR specular reflection data whereas the slate surface produces diffuse reflection data more typical of most expected deployment conditions. Reflectance data were taken at 60^o incidence angle from the bare surfaces and after the addition of approximately 3.3 g/m^2 and 10 g/m^2 of the simulant SF96 to about half the surface. To provide the required thermal contrast with the ambient temperature background, both reflection data from a quartz lamp (indoor) and the natural sky (outdoor) were taken. Figure 11 illustrates the indoor test configuration. The rather high incidence angle was used to maximize the difference in the reflectances at the S and P polarizations. Figures 12 and 13 show the equipment positioning for the indoor testing. The wavelength scan time was 1.5 s per data cube.

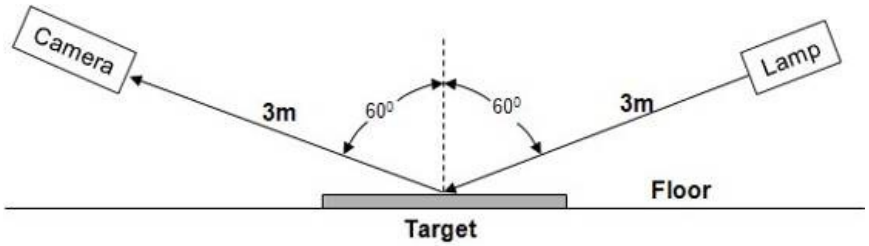

Figure 11. Test configuration used in the data collection at the Telops facility.

Figure 12. Test configuration with quartz lamp and Al target.

Figure 13. Test configuration facing Hyper-Cam.

3.2 Processing the Hyper-Cam data

Figures 7 and 8 above show the spectral and spatial components from unmixing Hyper-Cam data from adding 3.3 g/m^2 of SF96 to Al at S polarization. The SF96 on Al reflectance component (lowest curve in Figure 7) was combined with the reflectance at P polarization to estimate the refractive index of SF96 within spectral windows centered at 7.9 μm and 9.5 μm. The estimates for 3.3 g/m^2 and 10 g/m^2 are shown in Figures 14 and 15 together with the spectral library indices of SF96. We see good agreement within the spectral windows.

Figures 16 and 17 show the spectral and spatial components from unmixing Hyper-Cam reflectance data collected indoors at S polarization from 3.3 g/m^2 of SF96 on slate. The diffuse reflectance of slate is more like that of natural surfaces such as roads or soil than Al. It reduces the signal amplitudes of the data and substantially modifies the reflectance of the SF96 as seen in Figure 16 and the left plot of Figure 17. However, combining the SF96 on slate component with the corresponding P polarization reflectance data gives reasonably good windowed refractive index estimates of SF96 in Figures 18 (3.3 g/m^2) and Figure 19 (10g/m^2).

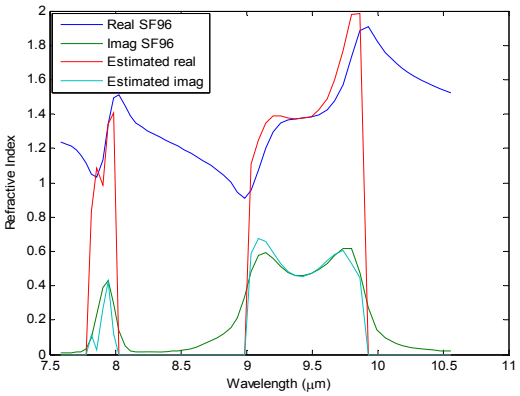

Figure 14. SF96 refractive index from 3.3 g/m^2 on Al.

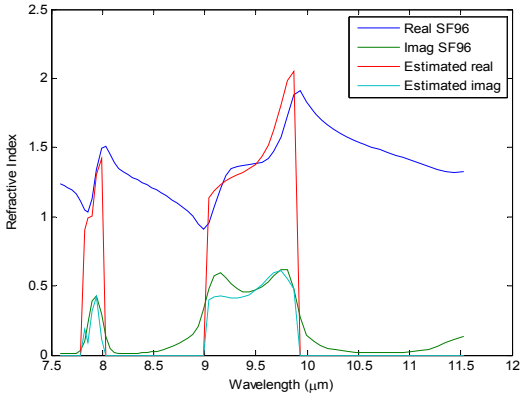

Figure 15. SF96 refractive index from 10 g/m^2 SF96 on Al.

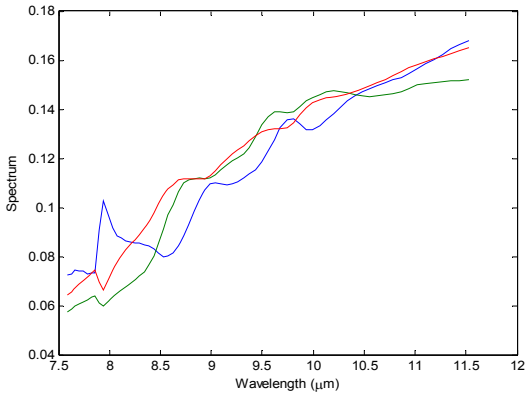

Figure 16. Spectral components for 3.3 g/m^2 of SF96 on slate at S polarization.

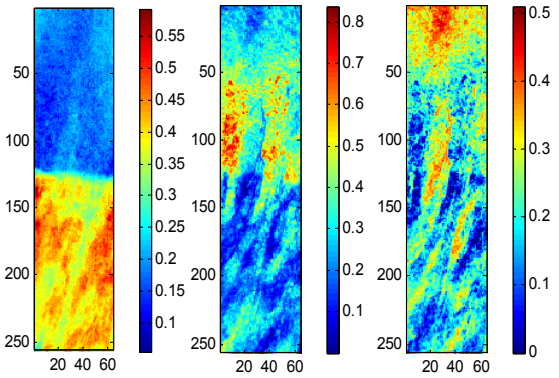

Figure 17. Spatial components for 3.3 g/m^2 of SF96 on slate at S polarization.

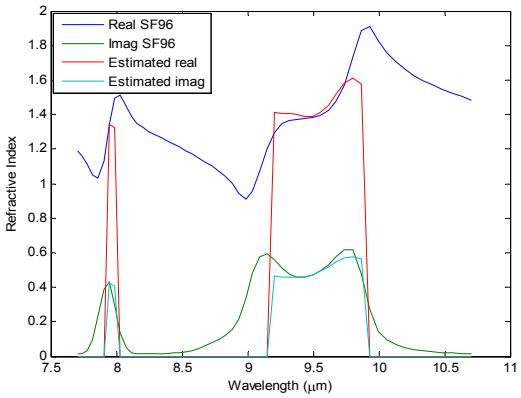

Figure 18. SF96 refractive index from 3.3 g/m^2 on slate.

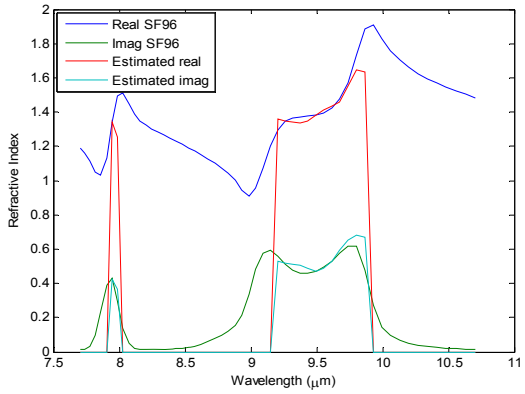

Figure 19. SF96 refractive index from 10 g/m^2 on slate.

4. SUMMARY

Over the past two years we have developed a new approach for detecting and identifying the presence of liquid chemical contamination on surfaces using hyperspectral imaging data. This work uses a new algorithm for unmixing the data to separate the liquid contamination component of the data from all other possible spectral effects such as the illumination and reflectance spectra of the pure background. Data from the Telops Hyper-Cam sensor at S and P polarization were used to estimate the liquid complex refractive index in spectral regions chosen to minimize interference from spectral structure of the background. We discussed our refractive index estimation approach, and showed results from tests conducted at the Telops facility in Québec under a contract with the U.S. Army Edgewood Chemical Biological Center. Those tests demonstrate the feasibility of the approach for liquid material identification on both specular and diffuse surfaces without the need for prior measurements of the uncontaminated surface reflectance.

ACKNOWLEDGMENT

This work was funded under DBC Technology Corp. Contract W911SR-13-C-0053 Advanced Real-Time Surface Contamination Sensor SBIR Phase I, and has been approved for public release; distribution unlimited.

REFERENCES

[1] Petryk, M. W. P., "Promising spectroscopic techniques for the portable detection of condensed-phase contaminants on surfaces," Applied Spectroscopic Reviews, 42(3), 287-373 (2007).

[2] Warren, R., and Osher, S., "Hyperspectral unmixing by the alternating direction method of multipliers," to appear in Inverse Problems and Imaging (2015).

[3] Harig, R., Braun, R., Dyer, C., Howle, C., and Truscott, B., "Short-range remote detection of liquid surface contamination by active imaging Fourier transform spectroscopy," Optics Express, 16(8), 5708-5714 (2008).

[4] Born, M., and Wolf, E., [Principles of Optics], 4th Ed., Pergamon Press, Oxford (1970).

[5] Thériault, J.-M., Lavoie, H., Puckrin, E., and Bouffard, F., "Passive standoff detection of surface contaminants: a novel approach by differential polarization FTIR spectrometry," 18(2), 251-262 (2008).